

Contents lists available at ScienceDirect

Comput. Methods Appl. Mech. Engrg.

journal homepage: www.elsevier.com/locate/cma





Investigating an extended multiphase flow model that includes specific interfacial area

Mohammad Ebadi ^{a,*}, James McClure ^b, Peyman Mostaghimi ^a, Ryan T. Armstrong ^{a,*}

- ^a School of Minerals and Energy Resources Engineering, The University of New South Wales, Sydney, Australia
- ^b National Security Institute, Virginia Tech, Blacksburg, VA 24061, USA

ARTICLE INFO

Keywords: Capillary pressure Specific fluid/fluid interfacial area Continuum-scale simulation Hysteresis Multiphase flow Porous media

ABSTRACT

Niessner and Hassnaizadeh (2008) proposed a set of governing equations to model multiphase flow in porous media based on first principles that includes fluid/fluid specific interfacial area as a state variable. Herein, we shed light on the lesser-discussed aspects of their proposed model, referred to as the extended model. Firstly, we show how the extended model facilitates real-time tracking of specific interfacial area. Secondly, we compare numerical solutions of the extended model to that of the traditional multiphase flow model with capillary dispersion and the analytical Buckley-Leverett solution. Thirdly, we provide a sensitivity analysis for the additional unknown parameters of the extended model - specific interfacial permeability and specific interfacial area generation. Lastly, a stability analysis is performed for the numerical solutions. As an auxiliary outcome, we provide an approach to solve the non-linear partial differential equations of the extended model by using torch.autograd as the automatic differentiation engine of PyTorch. Our results demonstrate that the extended model can provide saturation profiles similar to those generated by traditional models, but with the added benefit of real-time tracking of specific interfacial area. The generated specific interfacial area profiles were comparable to expected trends from previous numerical and experimental studies and highlighted the importance of the capillary pressure relationship and specific interfacial area generation term. The results also demonstrate an important balance between the permeability of the porous media and the interfacial permeability that must be maintained; otherwise, generated profiles become physically unrealistic. Overall, the extended model explains the evolution of specific interfacial area during multiphase flow at the cost of additional non-linearity and unknown parameters.

1. Introduction

The study of immiscible multiphase flow in porous media is a critical research area with a wide range of applications in fields such as carbon capture and storage [1,2], geothermal energy production [3], unconventional resources management [4], underground coal gasification [5], and enhanced oil recovery [6]. To achieve significant advancements in these highlighted fields, a thorough understanding of how immiscible fluids interact during flow in porous media is essential [7]. Accordingly, numerical simulation is considered a powerful tool that not only provides researchers with insights into the underlying physical mechanisms but also enables them to analyze complex problems [8].

E-mail addresses: m.ebadi@unsw.edu.au (M. Ebadi), ryan.armstrong@unsw.edu.au (R.T. Armstrong).

https://doi.org/10.1016/j.cma.2023.116594

Received 25 July 2023; Received in revised form 2 November 2023; Accepted 3 November 2023

Available online 7 November 2023 0045-7825/© 2023 The Author(s). Published by Elsevier B.V. This is an open access article under the CC BY license (http://creativecommons.org/licenses/by/4.0/).

^{*} Corresponding authors.

Capillary pressure (p_c) is a key parameter in the numerical simulation of immiscible multiphase flow in porous media [9]. It is defined as the pressure difference between two immiscible fluids in a porous medium [10]. At the continuum-scale, p_c is traditionally calculated as a function of wetting phase saturation, $p_c = f(S_w)$ [11]. Even though this is an oversimplified model that cannot logically describe the hysteresis phenomena (non-uniqueness solution for p_c) [12,13], it remains widely used in numerical models. This is due to its simple nature that only depends on one unknown (S_w) in the continuum-scale modeling of multiphase flow in porous media [14].

Regarding the p_c hysteresis phenomenon, significant efforts have been made to address the associated ambiguity [15–17]. The pioneering thermodynamic approach developed by Hassnaizadeh and Gray in early 1990s suggests that including interfacial area can resolve the non-uniqueness issue in the case of capillary pressure models [18–21]. This theory is based on developing a model that explicitly accounts for the effects of interfaces in a multiphase system. As a result, the classic p_c relationship is modified to $p_c = f(S_w, a_{wn})$, where a_{wn} represents the specific fluid/fluid interfacial area [22,23]. The theory proposes a surface that represents all possible combinations of p_c , S_w and a_{wn} [24], which can be mathematically described by bi-quadratic functions [25], or even physical-based range models [26]. In essence, the classic $p_c = f(S_w)$ relationship can be viewed as an artifact of projecting the 3D surface of $p_c - S_w - a_{wn}$ onto the $p_c - S_w$ plane [27,28].

Previous studies indicate that incorporating a_{wn} into a p_c model can almost remove the hysteresis effect [27,29–32]. Continuing from a geometric standpoint, the $p_c - S_w - a_{wn}$ surface provides a reasonable description of the fluid configuration in a porous medium; however, its accuracy may not be optimal as previous studies have revealed that hysteresis can still occur under specific conditions [33–35]. More recent research has shown that by considering a fluid in a porous medium as a 3D connected body in space, its configuration can be achieved by a hyperobject of $p_c - S_w - a_{wn} - \chi$ [36], where χ stands for the Euler characteristic and defined as the average measure for the connectivity of the fluid body [37]. To put it simply, it can be stated that p_c is unique defined by $f(S_w, a_{wn}, \chi)$ [38,39].

While developing new capillary pressure relationships based on additional geometrical terms is academically interesting, a key question remains in regards to the incorporation of such a relationship into a multiphase flow model [35,40]. The governing equations of the classical multiphase flow model neither describe the evolution of a_{wn} [41] nor accounts for χ [42], it is therefore impossible to use $p_c = f(S_w, a_{wn}, \chi)$ or $p_c = f(S_w, a_{wn})$. The reason behind this is that the classic multiphase flow model (referred to as the *classic model* from hereon) does not explicitly account for the effects of interfaces [18], and the geometric description of the system [43]. However, based on previous theoretical works and certain simplifying assumptions, the classic model can be extended with an additional governing equation for the evolution of a_{wn} [44–46]. This makes it possible to use $p_c = f(S_w, a_{wn})$ as a constitutive model with almost zero hysteresis.

While the model proposed by Niessner and Hassanizadeh [44] (referred to as the extended model from hereon) incorporates the $a_{wn} - p_c - S_w$ surface, it is not entirely clear how the parameters of the additional governing equation affect the model results. Furthermore, the extended model is highly nonlinear and dealing with this nonlinearity to find an appropriate solution strategy remains uncertain. Therefore, our aim is to investigate the extended model to gain a better understanding of it. In this regard, Section 2 briefly reviews the mathematical aspects of the classic and extended models. Moreover, the section provides details on how to solve the extended model and manage its nonlinearity using torch.autograd function of torch library in Python. Next, a physical model representing a typical porous media is described. Section 3 first presents and discusses the generated results. Then, a sensitivity analysis is performed to determine the importance of the parameters of the new governing equation in the extended model. Lastly, the run-time and relative errors are analyzed as useful indices for evaluating and optimizing the computational cost. In conclusion, Section 4 highlights the importance of the extended model, and the possible challenges.

2. Methodology

Before delving into the mathematical background of the *classic* and *extended models*, it is necessary to consider the assumptions that are considered by previous researchers and relevant to the work presented herein [10,45,47]. The following assumptions apply:

- · One-dimensional immiscible flow occurs for two incompressible fluids.
- Flow is horizontal, and the effect of gravity is not taken into account.
- · Viscosities are constant.
- · Homogeneous and isotropic porous medium rock.
- · Porosity remains constant over time.
- The porous medium is perfectly wettable by the wetting phase.
- The interfacial mass density is assumed to be constant.
- · Only wetting phase is injected from the inlet face.
- · The considered physical system is isothermal.
- The only driving force for the flow of phases is the pressure gradient; further, the driving force for the interfaces is the gradient of a_{wn} . The standard Darcy's law is assumed to hold.

Based on these assumptions, it is possible to compare the classic model and extended model.

2.1. Classic model

Using the mass conservation law and applying Darcy's law, the system of equations for the *classic model* can be expressed as follows [48].

$$\phi \frac{\partial S_w}{\partial t} + \frac{\partial}{\partial x} \left(-\frac{k_{rw}k}{\mu_w} \frac{\partial p_w}{\partial x} \right) = \frac{q_w}{V_b} \tag{1}$$

$$\phi \frac{\partial S_n}{\partial t} + \frac{\partial}{\partial x} \left(-\frac{k_{rn}k}{\mu_n} \frac{\partial p_n}{\partial x} \right) = \frac{q_n}{V_b} \tag{2}$$

$$S_w + S_n = 1 \tag{3}$$

$$p_c = p_n - p_w \tag{4}$$

where ϕ is porosity, k is permeability (m²), μ_w and μ_n represents the viscosities of wetting and non-wetting phases (Pa s), k_{rw} and k_{rn} are the relative permeabilities of wetting and non-wetting phases, q_w and q_n indicate the injection rates of wetting and non-wetting phases (m³ s⁻¹), V_b is the bulk volume of the control element (m³), S_n is the non-wetting phase saturation, $\frac{\partial S_w}{\partial t}$ and $\frac{\partial S_n}{\partial t}$ stand for the changes of wetting and non-wetting saturation with respect to time (s⁻¹), p_w and p_n are the pressures of wetting and non-wetting phases (Pa), and finally $\frac{\partial p_w}{\partial x}$ and $\frac{\partial p_n}{\partial x}$ are the pressure gradients of wetting and non-wetting phases (Pa m⁻¹).

The system includes two nonlinear second-order Partial Differential Equations (PDEs), one for each of the two phases. The reason for the poslinearity is the decorder partial v_n and v_n are the pressure of the two phases.

The system includes two nonlinear second-order Partial Differential Equations (PDEs), one for each of the two phases. The reason for the nonlinearity is the dependency of $k_{r_w/n}$ to S_w which is changed by changes of p_w/n . Next, Eqs. (3) and (4) are employed to couple Eqs. (1) and (2). As a result, S_w and p_n are considered as the primary unknowns, and S_n and p_w are the secondary unknowns [14]. The reason for selecting S_w and p_n as the primary unknowns adheres to established conventions detailed in the provided reference. Moreover, p_c can be calculated with the help of a traditional p_c model based on S_w [49]. In this study, p_c is calculated based on the following model [50]:

$$p_c = p_{th} \left(\frac{S_w - S_{wi}}{1 - S_{wi}} \right)^{-\frac{1}{\lambda}} \tag{5}$$

where λ is introduced as the pore size distribution index, p_{th} (Pa) is threshold pressure, and S_{wi} is the irreducible wetting phase saturation. Also, k_{rn} and k_{rw} are given by [50]:

$$k_{rn} = k_{rn_{Swi}} \left(\frac{1 - S_w - S_{nr}}{1 - S_{wi} - S_{nr}} \right)^{N_n} \tag{6}$$

$$k_{rw} = k_{rw_{Snr}} \left(\frac{S_w - S_{wi}}{1 - S_{wi} - S_{nr}} \right)^{N_w} \tag{7}$$

here, the residual non-wetting phase saturation is S_{nr} . Also, N_w and N_n are known as Corey exponents. The end point at S_{wi} is k_{rno} , and at S_{vr} is k_{rwo} .

 $k_{rn_{Swi}}$, and at S_{nr} is $k_{rw_{Snr}}$.

The Initial Conditions (ICs) are a uniform pressure of the non-wetting phase throughout the physical model and the wetting-phase saturation is equal to S_{nvi} .

$$p_n(x) = p_i, \qquad \forall x \in [0, L)$$

$$S_m(x) = S_{mi}, \qquad \forall x \in (0, L]$$
(8)

where p_i is the initial pressure of the non-wetting phase, and L is the length of the physical model (m). Furthermore, for imbibition, the inlet face is subject to a constant-flow boundary (Neumann boundary condition) with a constant injection rate of the wetting phase $(q_{w_{inj}})$, where S_w reaches its maximum possible value which is $1 - S_{nr}$. The outlet face has a constant pressure boundary (Dirichlet boundary condition) with a constant back pressure (p_b) [14,51]. These Boundary Conditions (BCs) can be expressed mathematically as follows:

At the inlet face:

$$q_{w_{(x=0)}} = q_{w_{inj}}$$
, (9)
 $S_{w_{(x=0)}} = 1 - S_{nr}$.

At the outlet face:

$$p_{n_{(x=L)}} = p_b$$
 (10)

To numerically solve the coupled PDEs, Taylor series expansion can be utilized for the discretization of the coupled PDEs [52]. To eliminate nonlinearity, the IMplicit Pressure Explicit Saturation (IMPES) method is used [53,54]. Additionally, the transmissibility terms between adjacent gridblocks are determined using the Single-Point Upstream Weighting (SPUW) approach [55]. The result is a system of linear simultaneous algebraic equations. More details about coupling, discretization, implementation of the IMPES method, the SPUW approach, and the applied solver are described in Appendix A.1.

Moreover, the advancement of the wetting phase in a porous medium can analytically be tracked based on the integration of the Buckley–Leverett equation [56]. It is important to note that the Buckley–Leverett equation does not consider the effects of p_c , assuming $p_c = 0$. However, it provides an analytical solution of where the front should be. The Buckley–Leverett equation is expressed as:

$$(X)_{S_w} = \frac{q_w t}{\phi A} \left(\frac{\mathrm{d}f_w}{\mathrm{d}S_w}\right)_{S_w} \tag{11}$$

where $(X)_{S_w}$ is the distance from the inlet face for any given S_w (m), t is time (s), A is cross-sectional area (m²), and $\left(\frac{df_w}{dS_w}\right)_{S_w}$ is the slope of the f_w versus S_w curve at S_w , where f_w for the displacement of non-wetting phase by wetting phase for a horizontal displacement and neglecting the capillary pressure gradient is:

$$f_w = \frac{1}{1 + \frac{k_{rn}\mu_w}{k_{rw}\mu_n}} \,. \tag{12}$$

2.2. Extended model

Based on the developed thermodynamic theory of two-phase flow in a porous medium [57] and considering the aforementioned assumptions, the extension to the system of equations for the *classic model* are [44]:

$$\frac{\partial a_{wn}}{\partial t} + \frac{\partial}{\partial x} \left(-\kappa a_{wn} \frac{\partial a_{wn}}{\partial x} \right) = e_{wn} \frac{\partial S_w}{\partial t} \,, \tag{13}$$

$$a_{wn} = f(S_w, p_c). \tag{14}$$

where a_{wn} denotes the specific fluid/fluid interfacial area in units of (m⁻¹), κ represents the interfacial permeability (m³ s⁻¹), and e_{wn} (m⁻¹) is the specific interfacial area generation term based on temporal changes in S_w . Eqs. (1), (2), (13), (3), (4), and (14) form the system of equations for the *extended model*. Eq. (13) is a second-order nonlinear PDE that governs the evolution of a_{wn} . The nonlinearity is caused by the fact that the term $a_{wn} \frac{\partial a_{wn}}{\partial x}$ is a product of two dependent variables a_{wn} and its partial derivative $\frac{\partial a_{wn}}{\partial x}$ [58].

Regarding the $a_{wn}-p_c-S_w$ surface, it can alternatively be re-interpreted as a single-value function as Eq. (14). To generate the surface, the following procedure can be followed. Beginning with Eq. (5) and fixing λ , p_{th} is varied to obtain three curves that satisfy $p_c^I \leq p_c^M \leq p_c^D$, representing Imbibition (*I*), Midway (*M*), and Drainage (*D*), respectively. Then, the following relationship is used to compute a_{wn} for a given S_w [59] as:

$$a_{nn} = \alpha S_w \left(1 - S_w \right) + \beta S_w \tag{15}$$

where α and β are undetermined parameters. Next, β is taken as a constant and α is chosen such that $a_{wn}^I \leq a_{wn}^M \leq a_{wn}^D$. Finally, a bi-quadratic function is fit to the dataset that includes (S_w, p_c^I, a_{wn}^I) , (S_w, p_c^M, a_{wn}^M) , and (S_w, p_c^D, a_{wn}^D) to build the $a_{wn} - p_c - S_w$ surface.

The extended model has 5 unknowns: p_n , p_w , S_n , S_w , and p_c . By coupling of Eqs. (1) and (2), p_n , S_w , and p_c are the primary unknowns, and the secondary ones are S_n , and p_w . Like the classic model, the extended model has the same ICs as mentioned in Eq. (8), except for the fact that the initial values of p_c need to be determined. Therefore, the ICs for the extended model can be stated as:

$$p_{n}(x) = p_{i}, \qquad \forall x \in [0, L)$$

$$S_{w}(x) = S_{wi}, \qquad \forall x \in (0, L]$$

$$p_{c}(x) = p_{ci}. \qquad \forall x \in (0, L]$$

$$(16)$$

In addition to the BCs mentioned in Eq. (9) for an imbibition scenario, the p_c at the inlet face should be determined as:

$$q_{w_{(x=0)}} = q_{w_{inj}}$$
,
$$S_{w_{(x=0)}} = 1 - S_{nr}$$
,
$$p_{c_{(x=0)}} = p_{c0}$$
. (17)

The BCs at the outlet face has the same conditions as Eq. (10).

It should be emphasized that the appropriate values for p_{ci} and p_{c0} are challenging to determine. Specifically, e_{wn} and κ are nonlinear functions of S_w and $\frac{\partial S_w}{\partial x}$, and changes in S_w can affect p_c through the $a_{wn}-p_c-S_w$ surface. As a result, e_{wn} and κ can influence the values of p_c , and conversely, the values of p_c can affect e_{wn} and κ . Furthermore, it is difficult to determine e_{wn} and κ although pore-scale studies can provide some basic models [44]. In this study, e_{wn} is considered constant to investigate its impact. Similarly, due to a lack of information, κ is also assumed to be constant. The implemented numerical scheme to solve the *extended model* is discussed in the following section.

Table 1Details of the porous medium and simulation scenarios for a typical Decane/Brine system in a sandstone rock [66–68].

Property	Value	Property	Value
<i>L</i> (m)	5×10^{-2}	∆x (m)	2×10^{-3}
$q_{w_{inj}}$ (m ³ s ⁻¹)	1.39×10^{-9}	Δt (s)	1.5
A (m ²)	1×10^{-4}	p_i (Pa)	1.3×10^4
μ_w (Pa s)	1×10^{-4}	p_b (Pa)	8×10^{3}
μ_n (Pa s)	1×10^{-4}	λ	3
S_{wi}	0.2	p_{th} (Pa)	4×10^{2}
S_{nr}	0.3	e_{wn} (m ⁻¹)	1.05×10^{2}
N_n	3.2	κ (m ³ s ⁻¹)	1×10^{-13}
N_w	2.4	p_{ci} (Pa)	Eq. (5) $ _{S_w = S_{wi}}^{\forall x \in (0,L]}$
ϕ	0.2	p_{c0} (Pa)	Eq. (5) $\Big _{S_w=1-S_{gr}}^{x=0}$
k (m ²)	9.869233×10^{-13}	ϵ	10-12

2.3. Numerical scheme

The system of equations in the *extended model* can be solved numerically by discretization based on Taylor series expansion. With regard to the coupled Eqs. (1) and (2), the k_r terms are calculated based on the S_w from the previous time step. It must be reminded that it is not applicable for p_c because it is a primary unknown. By utilizing the SPUW approach, the first two algebraic equations for each gridblock are generated. Next, Eq. (13) is treated with the same discretization approach to generate the third algebraic equation for each gridblock. The resulting system of nonlinear simultaneous algebraic equations can be expressed mathematically as:

$$F(X) = 0, (18)$$

where F represents the system of nonlinear simultaneous algebraic equations. Further details on how to obtain the system of nonlinear simultaneous algebraic equations for the *extended model* are explained in Appendix A.2.

The appropriate values of X can be obtained by using a nonlinear solver like Newton's method [60]. Newton's method is a powerful iterative method that refines a set of Initial Guesses using the inverse Jacobian matrix (**J**), which is a matrix of partial derivatives of the equations with respect to their variables [61]. The refined solution is repeated until the condition of $F(\text{refined Initial Guesses}) \le \varepsilon$ is satisfied. ε is a very small value such as 10^{-12} [62]. Newton's method can be expressed as:

$$X_{new} = X_{old} - \mathbf{J}^{-1}(X_{old})F(X_{old}), \tag{19}$$

where X_{old} represents old solution at the previous time step, and X_{new} is the new solution at the current time step.

The bottleneck of using Newton's method to solve Eq. (18) is the formation of J. Since J is a dense matrix of partial derivatives, its computation can be expensive. Furthermore, J may be singular (having a determinant of zero), which can prevent the use of Newton's method. Additionally, J might be ill-conditioned, meaning that small changes in the input variables can result in large changes in the output variable, potentially leading to numerical instability or divergence [63]. To minimize the risks associated with forming J, one possible approach is to estimate J by numerically approximating the partial derivatives of a given function with respect to its inputs based on the finite difference method [64]. The current research uses the J=torch.autograd.functional.jacobian(F, X) command from the PyTorch library in Python [65]. The implemented numerical scheme to solve the system of equations for the extended model is illustrated in Fig. 1.

2.4. Physical model

To compare the results of the *extended model* with those of the *classic model*, a homogeneous and isotropic porous medium based on a typical Bentheimer core plug was used, see Table 1 [66–68]. Table 1 also includes details of the simulation scenarios used for the *classic model* and *extended model*. For the sake of comparison, the p_{ci} and p_{c0} as the BCs for the *extended model*, are assigned values generated by the p_c -model of the *classic model* for S_{wi} and $1 - S_{nr}$, respectively, as given by Eq. (5).

To acquire the desired saturation profiles for the *classic model*, it is necessary to have a p_c -curve. This p_c -curve for an imbibition scenario based on Eq. (5) is shown in Fig. 2(a). Similarly, Fig. 2(b) shows the k_r -curves according to Eqs. (6) and (7). In order to use Eq. (11) to analytically generate the saturation profiles for the classic model, it is required to generate the f_w -curve with respect to Eq. (12). As shown in Fig. 2(c), it should be noted that the shock front of the system under study has a f_w value of 0.85. Additionally, it can be inferred that S_w increases abruptly from 0.2 (S_{wi}) to 0.57 (S_{wf}), and the value of f_w' at S_{wf} , or $\left(\frac{\mathrm{d}f_w}{\mathrm{d}S_w}\right)_{Swf}=2.78$. The main concept behind the *extended model* is based on the $a_{wn}-p_c-S_w$ surface. As explained in Section 2.2, to satisfy the

The main concept behind the *extended model* is based on the $a_{wn}-p_c-S_w$ surface. As explained in Section 2.2, to satisfy the condition that $p_c^I \le p_c^M \le p_c^D$, three values of p_{th} , namely 4×10^2 Pa (I), 6×10^2 Pa (M), and 8×10^2 Pa (D), are considered to generate the necessary p_c -curves as illustrated in Fig. 3(a). Next, Eq. (15) can be employed with three values of α so that $a_{wn}^I \le a_{wn}^M \le a_{wn}^D$, see Fig. 3(b). Then, by using scipy.optimize.curve_fit [69] in Python, a bi-quadratic function is fitted to the obtained

Extended Model

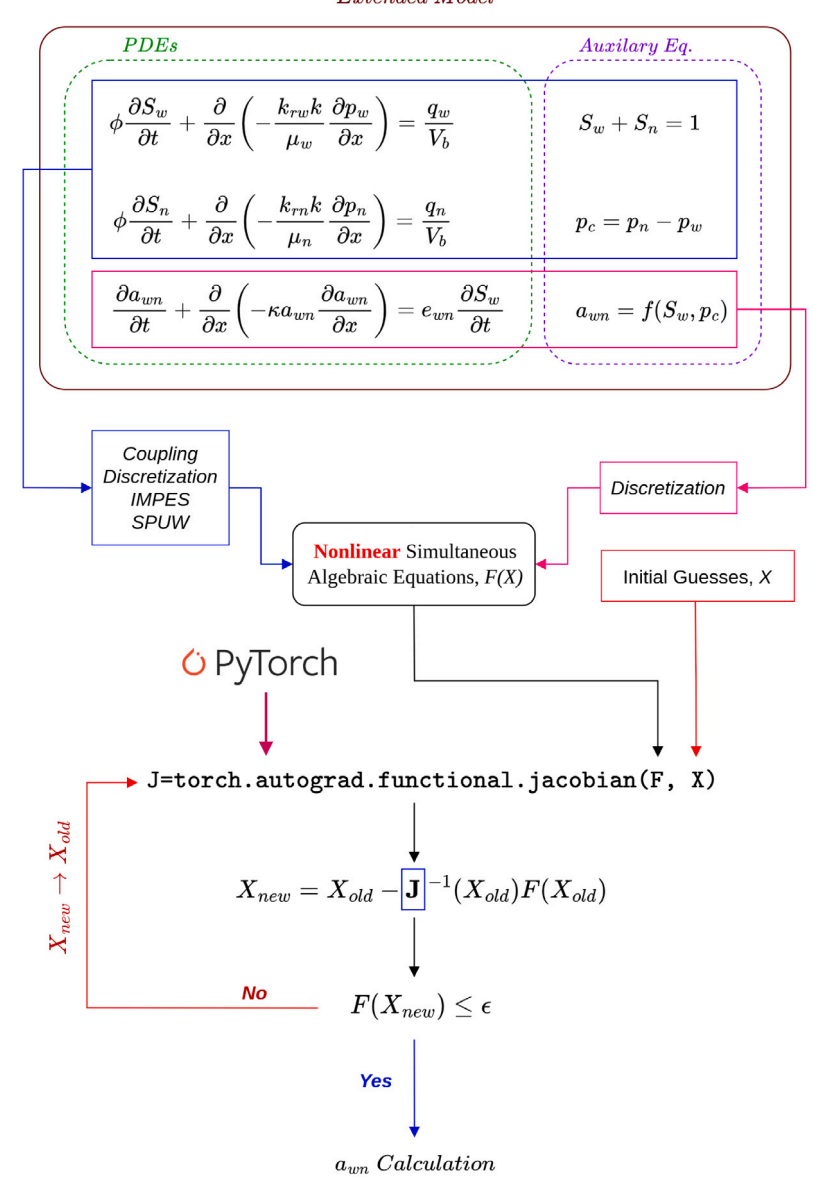


Fig. 1. The numerical scheme to calculate a_{wn} by solving to the system of equations for the extended model.

data, including (S_W, p_c^D, a_{wn}^D) , (S_W, p_c^M, a_{wn}^M) , and (S_W, p_c^I, a_{wn}^I) . The resultant surface is demonstrated with the viridis colormap in Fig. 3(c). The proposed model for $S_{wi} \leq S_w \leq 1 - S_{nr}$ $(R^2 = 0.98)$ is:

$$\begin{array}{lclcrcl} a_{wn} \left(S_w, p_c \right) & = & 1.39 \times 10^3 \times S_w & - & 3.16 \times 10^{-5} \times p_c^2 \\ & + & 6.11 \times 10^{-1} \times S_w \times p_c & - & 1.36 \times 10^3 \times S_w^2 \\ & + & 8.51 \times 10^{-2} \times p_c & - & 3.49 \times 10^2 \end{array} \tag{20}$$

In the system of equations for the extended model, all the a_{wn} terms in Eq. (13) are replaced by Eq. (20).

3. Results and discussions

This section presents a comparison between the *classic model* and *extended model*, followed by an investigation of the significance of e_{wn} and κ as the primary parameters of the *extended model*. Additionally, a sensitivity analysis with the number of gridblocks is conducted to investigate the stability of the implemented numerical scheme.

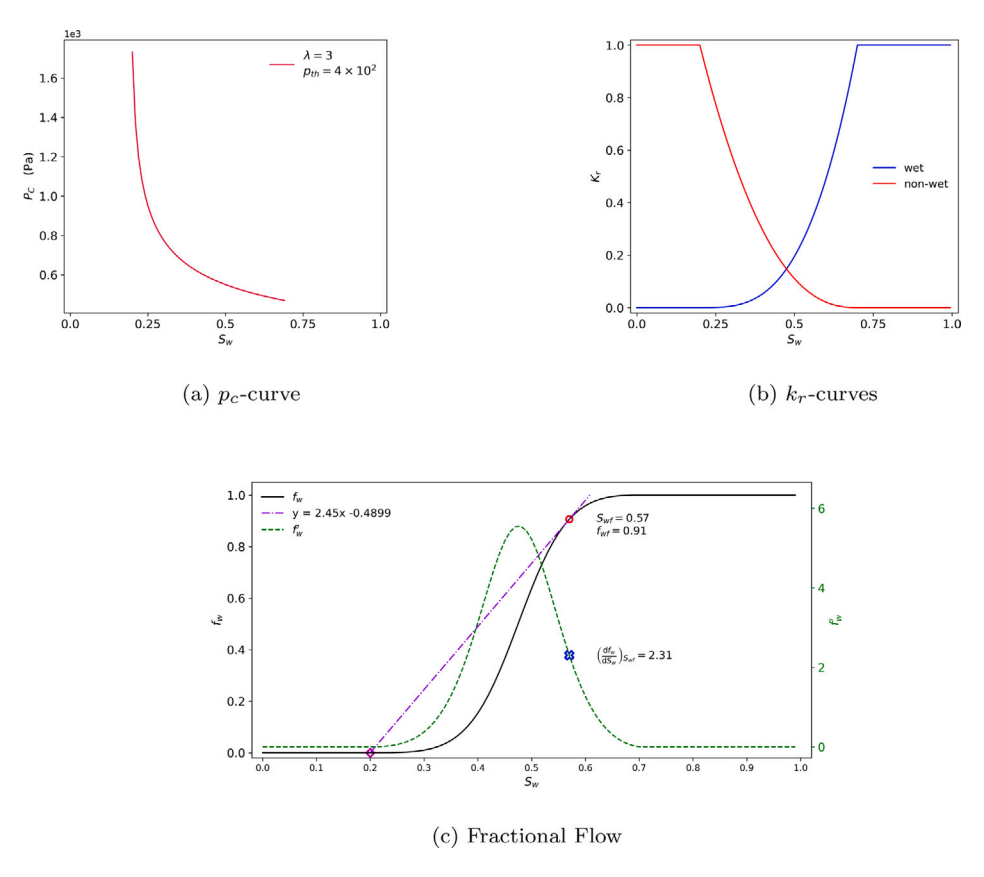


Fig. 2. Requirements to calculate saturation profiles for the classic model.

3.1. Simulation results

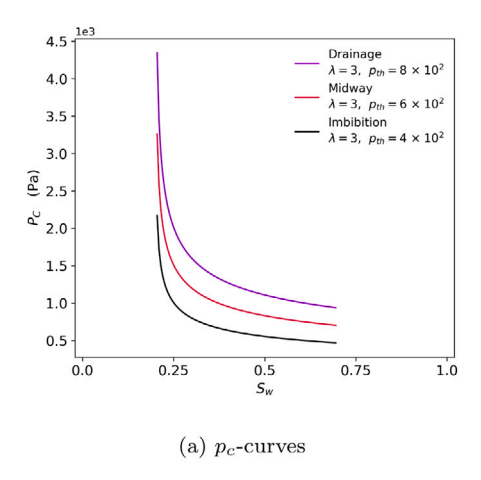
Based on the constitutive relationships shown in Fig. 2, the analytical and numerical S_w profiles for the *classic model* are presented in Fig. 4(a). The numerical S_w profiles are based on Eqs. (1), (2), (3), and(4), and the analytical S_w profiles are based on Eq. (11). The inclusion of p_c in the numerical solutions eliminates the shock fronts in the saturation profiles, resulting in a smooth dispersed trend of increasing S_w .

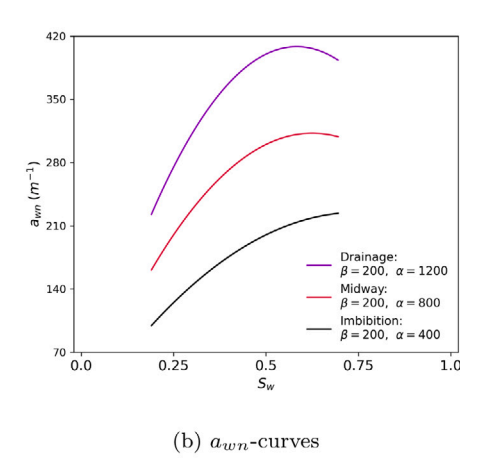
Using a nonlinear solver such as Newton's method, as described in Section 2.3, the system of equations for the *extended model* can be solved numerically to produce the desired profiles of S_w (Fig. 4(a)) and p_c (Fig. 4(b)). Utilizing Eq. (20) and referring to Figs. 4(a) and 4(b), the *extended model* allows for real-time tracking of the a_{wn} profiles (Fig. 4(c)). For comparison purposes, all profiles are presented based on dimensionless length, defined as $x_D = \frac{x}{L}$. As shown in Fig. 4(a), the numerically generated S_w profiles for the *extended model* (labeled as Ex) exhibit a high level of consistency with those generated by the *classic model* (labeled as C1).

In Fig. 4(b), as the front of the wetting-phase advances in the porous medium, both the C1 and Ex p_c profiles exhibit the expected imbibition trends: an increase in S_w at each gridblock leads to a reduction of p_c in the same gridblock, Fig. 4(b). However, in Fig. 4(b), the C1 p_c profiles are based on S_w data from the previous time step (IMPES implementation), and they are employed to generate the C1 S_w profiles in Fig. 4(a). Meanwhile, the Ex p_c profiles in Fig. 4(b) are computed simultaneously with the Ex S_w profiles in Fig. 4(a), based on numerical solution of the *extended model*, as described in Section 2.3. The main reason why both types of C1 and Ex are very similar to each other is that the $a_{wn} - p_c - S_w$ surface (Fig. 3) used in the *extended model* is based on the same p_c -curve used in the *classic model*.

In addition, as illustrated in Fig. 4(c), the *extended model* demonstrates the propagation and increase of a_{wn} as the Ex p_c profiles decrease and the Ex S_w profiles increase. This is expected because, by the advancement of the wetting phase in the porous medium, the surface area between the two phases increases [23,26]. The distribution of the calculated a_{wn} profiles are in strong agreement with those already reported [44]. However, Nordhaug et al. reported a_{wn} profiles that were bell-shaped and advanced from the inlet to outlet face [59]. In other words, in each gridblock, the a_{wn} approaches its maximum value and then decreases after the invading phase becomes dominant. But, Fig. 4(c) does not show such a distribution.

To figure out the reason for the difference behind our reported behavior and that reported by Nordhaug et al. [59], it is necessary to examine the trend of a_{wn} versus S_w , Fig. 5. According to the literature, the trend of a_{wn} versus S_w typically follows a hump-shaped





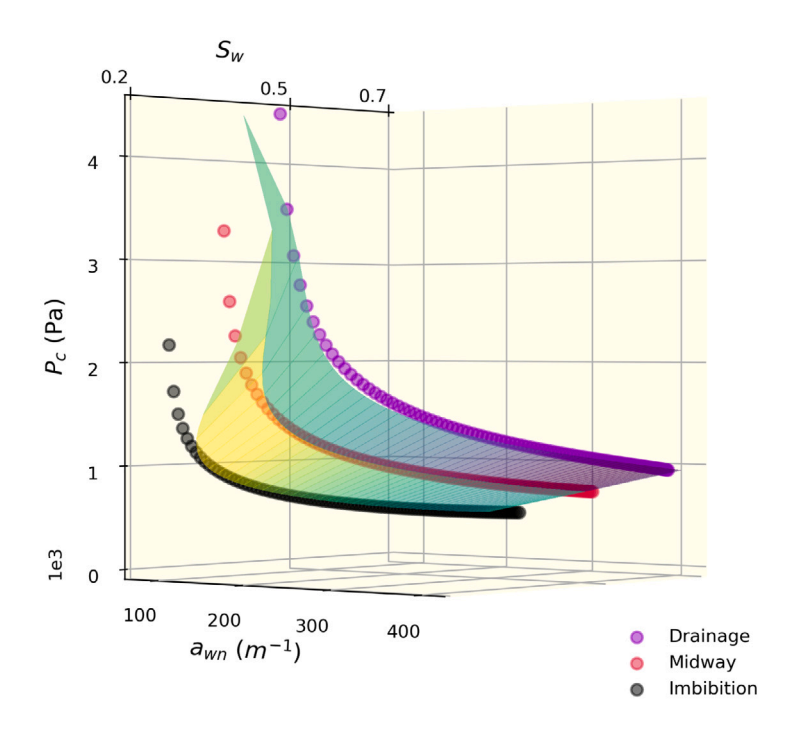


Fig. 3. The presented p_c -curves in (a) are combined with a_{uw} -curves in (b) to establish discrete data points of (S_w, p_c, a_{uw}) . These data points are subsequently utilized to fit a bi-quadratic function to form the desired surface as shown in (c)

(c) $a_{wn} - p_c - S_w$ surface

curve, with a critical saturation where a_{wn} values increase up to that point and then decrease afterward [39,70]. The same behavior can be observed in the contours of Fig. 5, which represent the $a_{wn}-S_w$ view of the $a_{wn}-p_c-S_w$ surface defined by Eq. (20). However, it is important to note that a large range of the S_w considered in this study (from $S_{wi}=0.2$ to $S_w=1-S_{nr}=0.7$) are lower than the critical S_w at which the corresponding a_{wn} reaches contour peak. This explains why the a_{wn} profiles consistently shows an increasing trend throughout this study. Furthermore, as the saturation S_w approaches its upper limit of 0.7, the relationship between a_{wn} and S_w exhibits a subtle shift in the trajectory on the $a_{wn}-p_c-S_w$ surface. This adjustment results in a change in the path followed by a_{wn} as it moves towards lower values, potentially forming a bell-shaped trend for a_{wn} profile. However, it is important to note that the limitations of the simulation scenario prevent the reflection of such behavior.

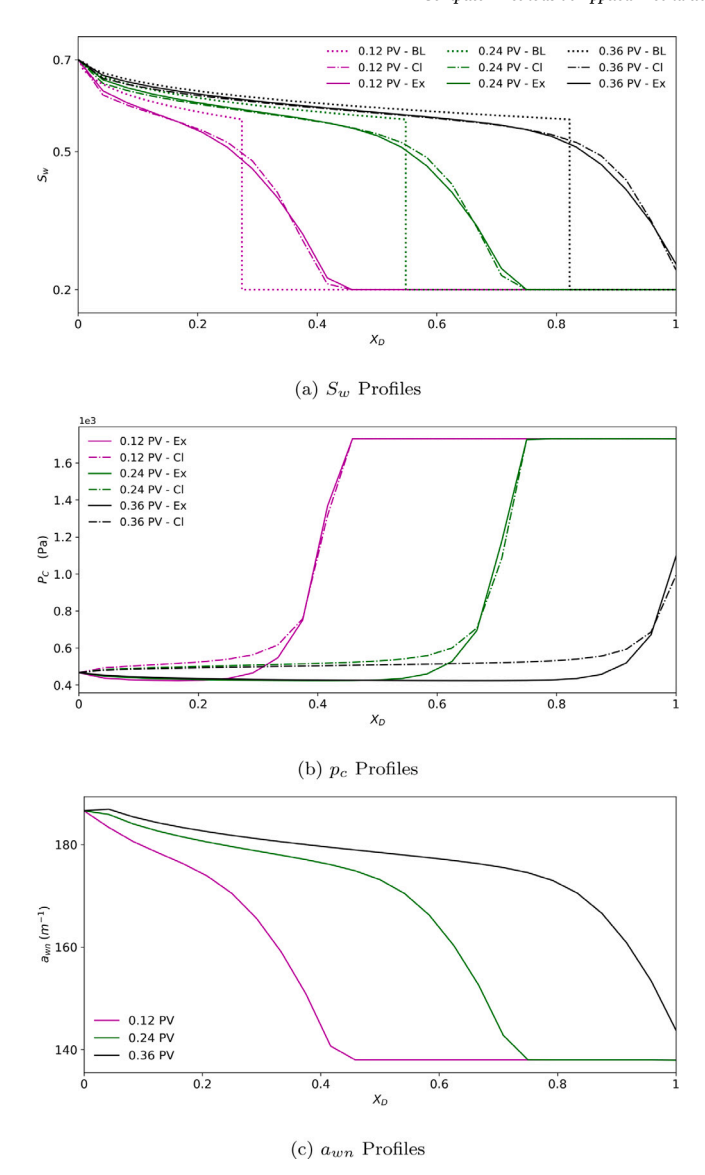


Fig. 4. classic model versus extended model based on injected Pore Volume (PV) and x_D .

3.2. Sensitivity analyses

Considering the generation term of a_{wn} based on temporal changes in S_w , it is expected that an increase in e_{wn} would lead to a corresponding increase in a_{wn} , while a decrease in e_{wn} would result in a decrease in a_{wn} . These trends are depicted in Fig. 6(a). It is worth noting that generated trends of a_{wn} exhibit a point of non-differentiability when varying e_{wn} . However, Eq. (13) includes the term $\frac{\partial a_{wn}}{\partial x}$, which implies that a_{wn} should be differentiable throughout the entire domain. The main reason for this discrepancy is the assumption of e_{wn} as constant, despite its dependence on S_w and $\frac{\partial S_w}{\partial x}$, as already discussed in Section 2.2. In more detail, the $a_{wn} - p_c - S_w$ surface suggests that changes in S_w result in a new value of a_{wn} based on its generation term or e_{wn} . Consequently, alterations in S_w lead to simultaneous variations in both a_{wn} and e_{wn} . However, maintaining a constant value for e_{wn} prevents a fully-dynamic interaction between a_{wn} and e_{wn} in response to changes in S_w . As a result, Fig. 6(a) illustrates that the expected trends have been generated according to the changes in e_{wn} although these changes have not been appropriately reflected in a smooth and differentiable manner.

Moreover, as evident from Figs. 6(b) and 6(c), the magnitude of changes in p_c is greater than that for changes in S_w . To gain a better understanding, it is necessary to examine the $p_c - S_w$ view of the $a_{wn} - p_c - S_w$ surface, as shown in Fig. 6(d). The contours derived from Eq. (20) indicate that changes in a_{wn} result in changes of p_c that are two to three orders of magnitude larger than the corresponding changes in S_w . Hence, variations in e_{wn} had a more pronounced impact on p_c compared to S_w .

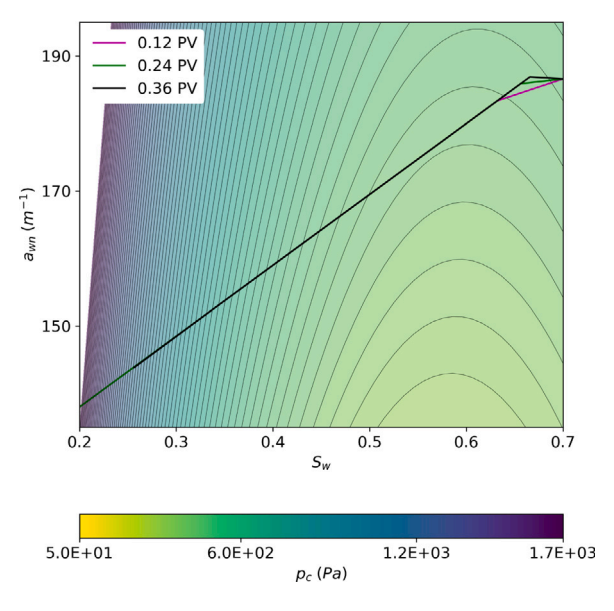


Fig. 5. Comparison of the implemented simulation scenario versus the $a_{wn}-p_c-S_w$ surface.

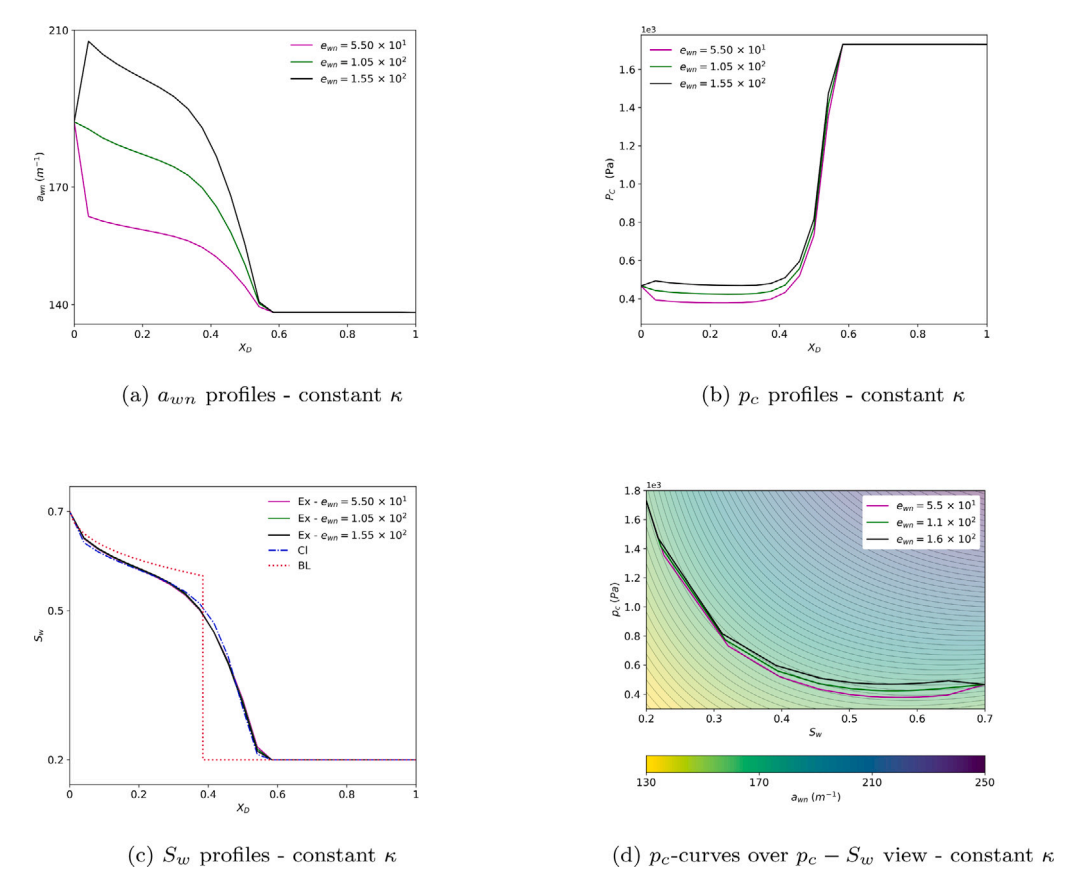


Fig. 6. The effects of e_{uvn} on the results of the extended model for $\kappa = 1 \times 10^{-13} \text{ m}^3 \text{ s}^{-1}$ and PV = 0.11.

Furthermore, the sharp increase followed by a tendency to stabilize in the a_{wn} profiles (Fig. 6(a)) can also be explained by examining the p_c -curves in Fig. 6(d). When S_w increases, there is a significant reduction in p_c , causing the p_c -curves to intersect a larger number of contours, resulting in a sharp increase in a_{wn} . However, as S_w surpasses 0.40, the reduction in p_c becomes less pronounced, leading to a smaller number of contour intersections and a slower increase in a_{wn} .

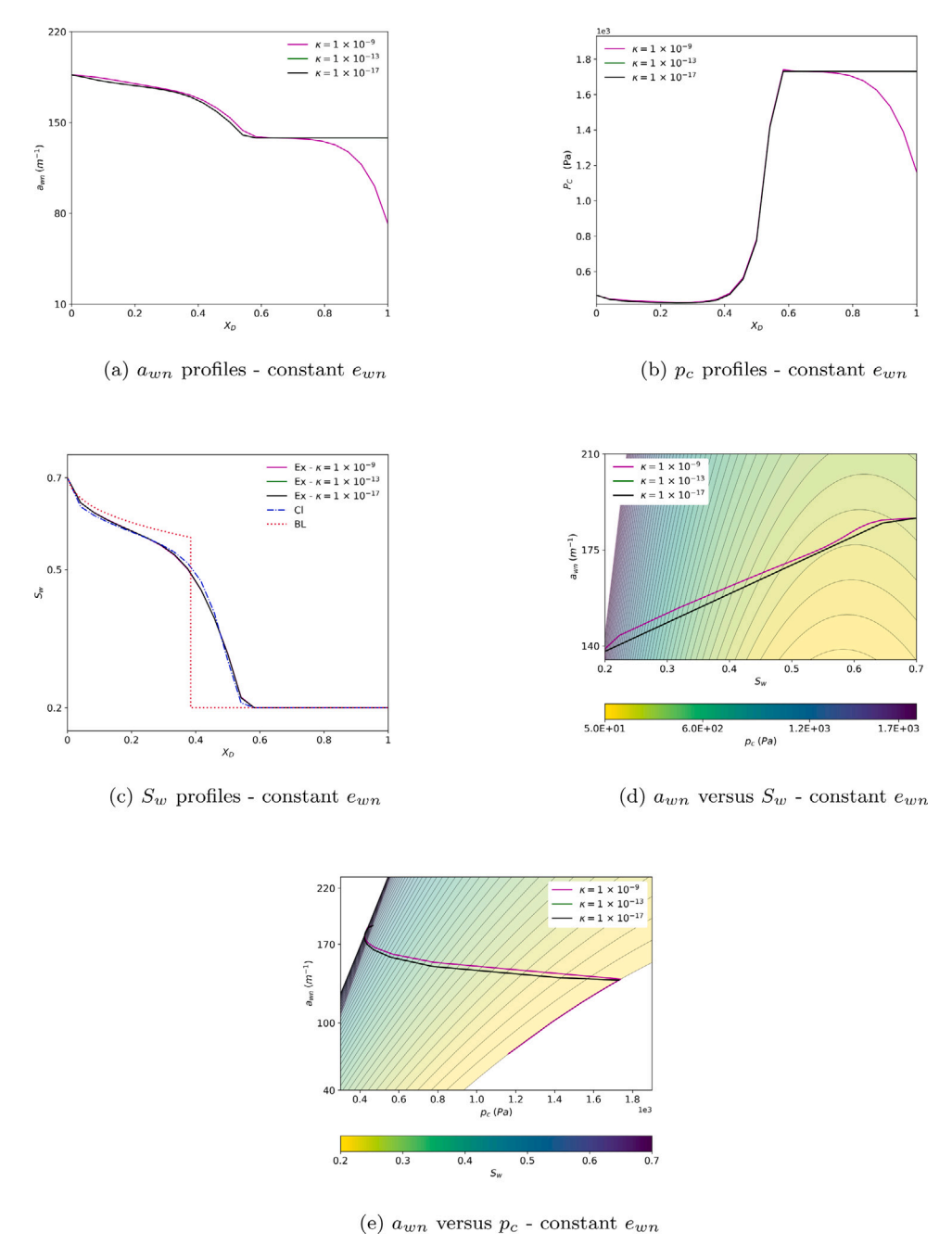


Fig. 7. The effects of κ on the results of the extended model for $e_{wn} = 1.05 \times 10^2 \text{ m}^{-1}$ and PV = 0.11.

Similarly, the effect of κ can be studied by keeping e_{wn} constant. In terms of analogy, κ plays the same role in Eq. (13) as k does in Eqs. (1) and (2). It means that k controls the advancement of S_w front, and κ controls the advancement of a_{wn} front. Although κ is assumed as a constant in this study, it is generally assumed to be a function of S_w and $\frac{\partial S_w}{\partial s_w}$. Also, S_w can effect a_{wn} through $a_{wn}-p_c-S_w$ surface. Therefore, it can be stated that because of the $a_{wn}-p_c-S_w$ surface, p_c reflects the balance between k and κ . From Figs. 7(a) and 7(c), it is evident that a decrease in κ does not disrupt the balance between the S_w and a_{wn} profiles. The advancements in both profiles remain aligned, indicating that there are no changes in the p_c profiles when κ is reduced from 1×10^{-13} m³ s⁻¹ to 1×10^{-17} m³ s⁻¹, Fig. 7(b). However, increasing κ from 1×10^{-13} m³ s⁻¹ to 1×10^{-9} m³ s⁻¹ disrupts the balance, causing the a_{wn} front to advance faster than the S_w front. This imbalance is evident in Figs. 7(a) and 7(c), where the profiles are no longer synchronized. The imbalance between k and κ is illustrated by the unusual trend of the p_c profile for $\kappa = 1 \times 10^{-9}$ m³ s⁻¹ in Fig. 7(b). The faster movement of the a_{wn} profile can only be supported by the p_c profile decreasing. This concept is further depicted

in Fig. 7(d), where the larger value of κ causes the $a_{wn} - S_w$ plot to overlap with contours of the $a_{wn} - p_c - S_w$ surface that have higher p_c values, Fig. 7(b). Next, After the peak, where S_w remains unchanged, the advancement of the a_{wn} front is only possible through a reduction in p_c . However, due to the geometry of the $a_{wn} - p_c - S_w$ surface, this reduction in p_c leads to a_{wn} values smaller than the initial condition, as shown in Fig. 7(e).

From a physical perspective, the rearrangement of fluids without changing S_w is possible due to capillary rearrangement. However, as simulated in the presented results, rearrangement of fluids far ahead of the saturation front where $S_w = S_{wi}$ is impossible because the wetting phase is immobile. Therefore, it can be concluded that although the $a_{wn} - p_c - S_w$ surface can mathematically handle the imbalance between k and κ , it can lack physical significance under specific conditions. Thus, the design of the $a_{wn} - p_c - S_w$ surface should incorporate the physical effects of this imbalance in order to accurately represent the system.

3.3. Computational costs

The system of equations governing the *extended model* is nonlinear. Discretizing the PDEs in that system generates a set of nonlinear algebraic equations that must be solved simultaneously. To optimize the computational cost and run-time of the solver, it is crucial to determine the optimal number of gridblocks. This number is directly related to the number of gridblocks (Appendix A.2) used in the discretization process. Fig. 8(a) illustrates the recorded run-time of solving the *extended model* based on the number of gridblocks ranging from 10 to 40. The run-time axis shows the average, minimum, and maximum run-time recorded for solving the extended model with 10 repetitions for 100 timesteps (Table 1). Also, the run-times have been determined using the Intel Xeon Gold 6230R processor operating at a clock speed of 2.10GHz. As expected, increasing the number of gridblocks results in longer run-time. Taking the results obtained for 40 gridblocks as the reference, it is possible to check the quality of the numerical solutions obtained for less gridblocks by computing the average relative error for each one of the primary unknowns. It can be inferred that when the number of gridblocks is 25 (as in this study), the averaged relative error for all the three unknowns is less than 2% in comparison with 40 gridblocks. But, the recorded averaged run-time is 2.2 times faster than the recorded averaged run-time for 40 gridblocks.

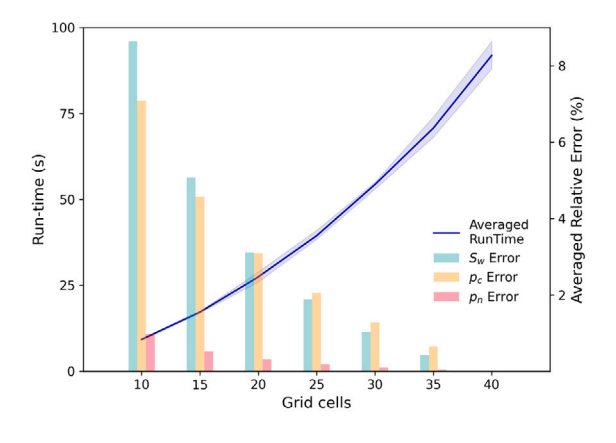
It is important to emphasize that the *extended model* can be readily tested with more than 40 gridblocks. However, it is not possible to compare the *classic model* with the *extended model* due to the numerical instability experienced by the *classic model* when the number of gridblocks exceeds 40 or when Δx is less than 1.25×10^{-3} m, if $\Delta t = 1.5$ s. For instance, Figs. 8(b) shows that when there are 41 gridblocks, the generated S_w profiles by the *classic model* are not numerically stable. The instability is due to the fact that using IMPES as the linearization in the *classic model* gives rise to a conditional stability, which is technically defined as the Courant–Friedrichs–Lewy (CFL) limit [71,72]. Regarding the implemented uniform discretization, the CFL states that the *classic model* produces numerically stable results if $CFL = ((q\Delta t) \cdot (2A\Delta x)^{-1}) < CFL_{max}$. CFL_{max} is a user-defined value that can be obtained by running the simulation until the instability appears [73]. Or, it can be said that CFL_{max} is the largest CFL in which *classic model* still performs numerically stable. Based on Table 1 and $\Delta x = 1.25 \times 10^{-3}$ m, CFL_{max} is 0.0083.

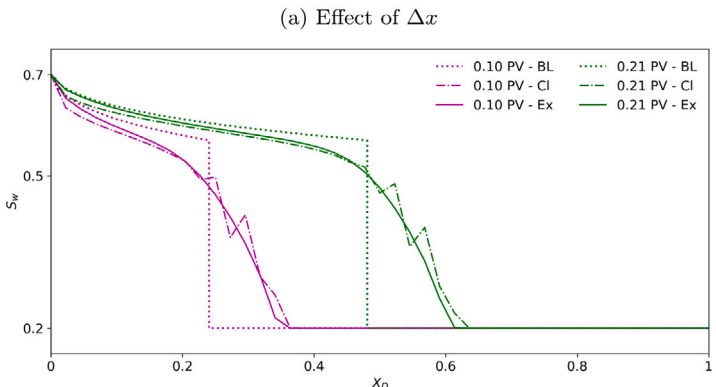
In the context of nonlinear solutions obtained using Newton's method, there is not a specific index similar to the CFL condition. The absence of a CFL-like condition for nonlinear systems is due to the fact that the stability analysis and convergence behavior of Newton's method are more complex and problem-dependent [74]. Instead, it is possible to observe the general trends of solutions based on the *extended model* by adjusting Δx or Δt based on the specific conditions given in Table 1, see Fig. 8(c). Based on the given Δx or Δt , if the computed results are meaningful, Convergence is achieved. If Newton's method generates results, but they are not physically possible, it can be inferred as numerical Instability, and if Newton's method cannot make any progress and fails to converge to a solution, it is considered as Divergence. Based on Table 1 and the $a_{wn} - p_c - S_w$ surface (Eq. (20)), the results of the *extended model* for $\Delta x < 6.66 \times 10^{-4}$ m when $\Delta t = 1.5$ s are not reliable. Likewise, it can be understood that stable results by the *extended model* are obtained when $\Delta t \le 5$ s if $\Delta x = 2 \times 10^{-3}$ m. It can be understood that if $\Delta x = 2 \times 10^{-3}$, the largest Δt that the *extended model* can have (5 s). It must be mentioned that the results for the effects of chosen Δt or Δx are based on running the simulation for 150 s.

4. Conclusions

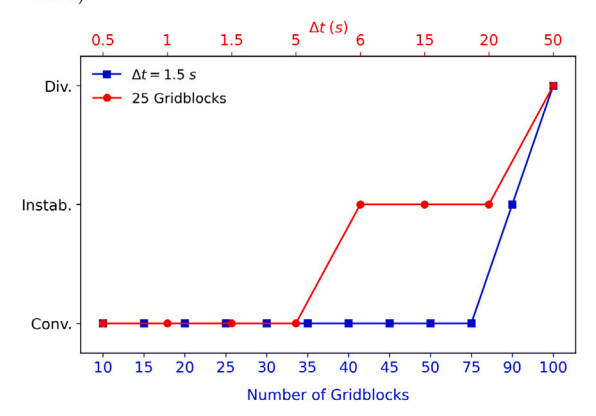
Traditionally, p_c is represented using an oversimplified model as $p_c = f(S_w)$. By considering the effects of a_{wn} on p_c , a $a_{wn} - p_c - S_w$ surface can be developed. The supposed surface can be interpreted as $p_c = f(S_w, a_{wn})$ which exhibits minimal hysteresis [23,26,28]. However, the *classic model* lacks the capability to incorporate this enhanced p_c model, whereas the *extended model* does possess this capability. By running numerical simulation scenarios based on the system of equations for the *extended model*, the following conclusions can be made:

- 1. Both the *extended model* and *classic model* provide nearly the same S_w profiles given a specific set of parameters while the *extended model* provides details on specific interfacial area that are consistent with those presented in the literature [39,44,70].
- The automatic differentiation using J=torch.autograd.functional.jacobian of PyTorch provides an approximate J for solving the nonlinear system of equations in the extended model.
- 3. The shape of the calculated a_{wn} profile strongly depends on the shape of the $p_c S_w a_{wn}$ surface and the specific simulation scenario. By adjusting S_{wi} and S_{nr} , it is possible to control the shape of the a_{wn} profile to be either piston-like [44] or bell-shaped [59].





(b) Comparison of stability between the extended model and the classic model for 41 gridblocks ($\Delta x \approx 1.22 \times 10^{-3} m$, and $\Delta t = 1.5 s$)



(c) Stability of *extended model*. Conv. stands for Convergence, Instab. means Instability, and Div. shows the Divergence

Fig. 8. Analyzing the computational cost and the numerical stability of extended model.

- 4. As a source term of a_{wn} , increasing or decreasing e_{wn} directly impacts the values of a_{wn} . Regarding the developed $p_c S_w a_{wn}$, changes in e_{wn} had a more significant effect on p_c values compared to S_w values.
- 5. The k controls the propagation of the S_w profile, and κ controls the propagation of the a_{wn} profile. If κ is too large, the a_{wn} profile advances faster than the S_w profile in the porous media. However, this is only possible if p_c changes, resulting in the generation of p_c profiles with unusual trends. Theoretically, κ is a function of S_w and $\frac{\partial S_w}{\partial x}$. Therefore, k and κ can be coupled, and the balance between them is nonlinear.

Overall, the extended model not only offers S_w profiles like the classic model but also incorporates an enhanced p_c model, enabling real-time tracking of a_{wn} profiles in porous media. Therefore, using the extended model provides an opportunity to compare the results of continuum-scale simulations with those obtained from pore-scale simulations. Future research can focus on modifying the extended model with representative parameters that can also be obtained from pore-scale simulations. This approach will help to bridge the gap between continuum-scale and pore-scale simulations, resulting in a more comprehensive understanding of immiscible multiphase flow in porous media.

Declaration of competing interest

The authors declare that they have no known competing financial interests or personal relationships that could have appeared to influence the work reported in this paper.

Data availability

No data was used for the research described in the article.

Appendix. Details of numerical solutions

A.1. Classic model

Eqs. (1) and (2) can be coupled using Eqs. (3) and (4) as follows.

$$\phi \frac{\partial S_w}{\partial t} + \frac{\partial}{\partial x} \left(-\frac{k_{rw}k}{\mu_w} \left(\frac{\partial p_n}{\partial x} - \frac{\partial p_c}{\partial x} \right) \right) = \frac{q_w}{V_b} \tag{A.1}$$

$$\phi \frac{\partial \left(1 - S_w\right)}{\partial t} + \frac{\partial}{\partial x} \left(-\frac{k_{rn}k}{\mu_n} \frac{\partial p_n}{\partial x} \right) = \frac{q_n}{V_b} \tag{A.2}$$

Rearranging Eqs. (A.1) and (A.2) and expressing them on a per unit bulk volume basis yields [55]:

$$\frac{kA}{\mu_w} \frac{\partial}{\partial x} \left(k_{rw} \left(\frac{\partial p_n}{\partial x} - \frac{\partial p_c}{\partial x} \right) \right) \Delta x = V_b \phi \frac{\partial S_w}{\partial t} - q_w \tag{A.3}$$

$$\frac{kA}{\mu_n} \frac{\partial}{\partial x} \left(k_{rn} \frac{\partial p_n}{\partial x} \right) \Delta x = V_b \phi \frac{\partial \left(1 - S_w \right)}{\partial t} - q_n \tag{A.4}$$

where Δx (m) stands for the length of the control element. By applying the IMPES linearization and using the numerical differentiation based on Taylor series expansion, Eqs. (A.3) and (A.4) can uniformly be discretized into a certain number (N) of block-centered gridblocks each one has a volume of V_h , and transformed into a system of algebraic equations as shown below.

$$\frac{kA}{\mu_{w}} k_{rw}^{m} \left(\frac{p_{n_{i+1}}^{m+1} - 2p_{n_{i}}^{m+1} + p_{n_{i-1}}^{m+1}}{\Delta x} - \frac{p_{c_{i+1}}^{m} - 2p_{c_{i}}^{m} + p_{c_{i-1}}^{m}}{\Delta x} \right) = V_{b} \phi \left(\frac{S_{w_{i}}^{m+1} - S_{w_{i}}^{m}}{\Delta t} \right) - q_{w} \tag{A.5}$$

$$\frac{kA}{\mu_n} k_{rn}^m \left(\frac{p_{n_{i+1}}^{m+1} - 2p_{n_i}^{m+1} + p_{n_{i-1}}^{m+1}}{\Delta x} \right) = V_b \phi \left(\frac{S_{w_i}^m - S_{w_i}^{m+1}}{\Delta t} \right) - q_n \tag{A.6}$$

where Δt is the time step (s). The second-order spatial derivatives are approximated using the central-difference method, and the first-order temporal derivative is approximated using the backward-difference method. The IMPES linearization method is employed to compute the saturation-dependent parameters based on the saturation values from the previous time step, and the pressures are computed at the current time step. The superscripts m+1 and m denote the current and previous time steps, respectively. Additionally, in the case of three adjacent gridblocks arranged in one-dimension, the subscripts i-1, i, and i+1 correspond to the indices of the left-side, central, and right-side gridblocks, respectively.

Eqs. (A.5) and (A.6) can be written for each of the gridblocks. Excluding the first and last gridblocks and considering the assumption that only wetting phase is injected from the inlet face, Eqs. (A.5) and (A.6) can be written as:

For 1 < i < N:

$$T_{w_{i,i+1}} \left(p_{n_{i+1}}^{m+1} - p_{n_i}^{m+1} \right) + T_{w_{i,i-1}} \left(p_{n_{i-1}}^{m+1} - p_{n_i}^{m+1} \right)$$

$$-T_{w_{i,i+1}} \left(p_{c_{i+1}}^m - p_{c_i}^m \right) - T_{w_{i,i-1}} \left(p_{c_{i-1}}^m - p_{c_i}^m \right)$$

$$-\zeta_{w_i} S_{w_i}^{m+1} + \zeta_{w_i} S_{w_i}^m + \mathcal{G}_{w_i}^{m} = 0$$
(A.7)

$$T_{n_{i,i+1}}\left(p_{n_{i+1}}^{m+1} - p_{n_i}^{m+1}\right) + T_{n_{i,i-1}}\left(p_{n_{i-1}}^{m+1} - p_{n_i}^{m+1}\right) + \zeta_{n_i}S_{w_i}^{m+1} - \zeta_{n_i}S_{w_i}^{m} + g_n^{\checkmark 0} = 0$$
(A.8)

where $\zeta_{w/n}$ as the accumulation coefficient $(\frac{m^3}{s})$ is:

$$\zeta_{w/n} = \frac{V_b \phi}{\Delta t} \tag{A.9}$$

The p_c^m values in Eq. (A.7) is computed with the help of a capillary pressure model based on the corresponding S_w^m values like Eq. (5). Taking the effects of uniform discretization and isotropic porous medium, T as the transmissibility ($m^3 Pa^{-1} s^{-1}$) between neighboring gridblocks is defined based on SPUW approach as [55]:

$$T_{w/n_{i,i\pm 1}} = \frac{1}{\mu_{w/n}} \times \frac{Ak}{\Delta x} \times k_{r_{w/n}} \left(S_{w_j}^m \right)_{\substack{j = \arg \max \left(p_{w/n_x}^m \right) \\ x \in \{i,j\pm 1\}}}$$
(A.10)

in which k_r data can be determined from Eqs. (6) and (7) based on S_w^m . The first gridblock is assigned the conditions stated in Eq. (9) due to the block-centered discretization. Therefore, S_{w_1} is already determined for all the time steps. As a result, the only primary unknown for the first gridblock is p_n , which can be computed by writing Eqs. (A.5) for i = 1 as follows:

$$T_{w_{1,2}} \left(p_{n_2}^{m+1} - p_{n_1}^{m+1} \right) - T_{w_{1,2}} \left(p_{c_2}^m - p_{c_1}^m \right)$$

$$-\zeta_{w_1} S_{w_1}^{m+1} + \zeta_{w_1} S_{w_1}^m + g_w^{q_{w_{inj}}} = 0$$
(A.11)

This means that the constant injection rate $q_{w_{inj}}$ can be treated as a source term in the first gridblock by using the *reflection technique* [14] at the left boundary of the inlet face between the imaginary zeroth (i = 0) and first (i = 1) gridblocks. Its value is then directly inserted into the equation instead of q_w .

Following the block-centered discretization, the last gridblock (i = N) is assigned the conditions stated in Eq. (10). As a result, Eqs. (A.5) and (A.6) can be written as:

$$T_{w_{N,N-1}}\left(p_{n_{N-1}}^{m+1} - p_{n_{N}}^{m+1}\right) - T_{w_{N,N-1}}\left(p_{c_{N-1}}^{m} - p_{c_{N}}^{m}\right)$$

$$-\zeta_{w_{N}}S_{w_{N}}^{m+1} + \zeta_{w_{N}}S_{w_{N}}^{m} + g_{w}^{m} = 0$$
(A.12)

$$T_{n_{N,N-1}}\left(p_{n_{N-1}}^{m+1} - p_{n_{N}}^{m+1}\right) + \zeta_{n_{N}}S_{w_{N}}^{m+1}$$

$$-\zeta_{n_{N}}S_{w_{N}}^{m} + g_{n}^{-\sqrt{2T_{n_{N}}\left(p_{n_{N}}^{m+1} - p_{b}\right)}} = 0$$
(A.13)

According to the *reflection technique*, the pressure boundary p_b at the outlet face between the last actual gridblock (N) and the imaginary adjacent gridblock (N+1) can be treated as a fictitious production term with a pressure of p_b . This term is located in the last actual gridblock but acts at a distance of $\frac{\Delta x}{2}$ from the center of the gridblock. This causes the coefficient of 2 for the transmissibility term, and the negative sign is due to its production mode [14].

All in all, by writing Eqs. (A.7), (A.8), (A.11), (A.12), and (A.13) for N gridblocks, a set of linear simultaneous algebraic equations including 2N-1 equations can be created and represented as:

$$AX = B \tag{A.14}$$

where $A_{2N-1\times 2N-1}$ is the tridiagonal matrix of coefficients, $B_{2N-1\times 1}$ is the matrix of answers, and $X_{2N-1\times 1}$ is the matrix of unknowns. To solve the linear system represented by Eq. (A.14), it is possible to use the X = numpy.linalg.solve(A,B) command from the numpy library in Python [75]. The results include N values of p_n and N-1 values of S_w at time step m+1.

A.2. Extended model

Eq. (13) can be rearranged as:

$$\frac{\partial a_{wn}}{\partial t} - \kappa \frac{\partial a_{wn}}{\partial x} \times \frac{\partial a_{wn}}{\partial x} - \kappa a_{wn} \frac{\partial^2 a_{wn}}{\partial x^2} = e_{wn} \frac{\partial S_w}{\partial t}$$
(A.15)

Utilizing the numerical differentiation based on Taylor series expansion, and regarding the uniform discretization, the discretized form of Eq. (A.15) per unit bulk volume is:

M. Ebadi et al.

$$V_{b} \frac{a_{wn_{i}}^{m+1} - a_{wn_{i}}^{m}}{\Delta t} - \kappa V_{b} \frac{a_{wn_{i+1}}^{m+1} - a_{wn_{i-1}}^{m+1}}{2\Delta x} \times \frac{a_{wn_{i+1}}^{m+1} - a_{wn_{i-1}}^{m+1}}{2\Delta x} - \kappa V_{b} a_{wn_{i}}^{m+1} \frac{a_{wn_{i+1}}^{m+1} - 2a_{wn_{i}}^{m+1} + a_{wn_{i-1}}^{m+1}}{\Delta x^{2}} = e_{wn} V_{b} \frac{S_{w_{i}}^{m+1} - S_{w_{i}}^{m}}{\Delta t}$$
(A.16)

Eq. (A.16), along with Eqs. (A.5) and (A.6), represents the discretized versions of Eqs. (13), (1), and (2), respectively. These equations constitute the main core of the system of equations for the *extended model*. It should be noted that Eqs. (A.5) needs to be modified for the use in the *extended model* in order that all values of p_c must be computed at the current time step with the superscript of m + 1, since p_c is a primary unknown in the *extended model*. Furthermore, Eq. (A.16) can be written as:

$$\zeta\left(a_{wn_i}^{m+1}-a_{wn_i}^m\right)$$

$$-T_{a_{wn}} \left(a_{wn_{i+1}}^{m+1^2} - 2a_{wn_{i+1}}^{m+1} a_{wn_{i-1}}^{m+1} + a_{wn_{i-1}}^{m+1^2} + a_{wn_{i-1}}^{m+1^2} + 4a_{wn_i}^{m+1} a_{wn_{i+1}}^{m+1} - 8a_{wn_i}^{m+1^2} + 4a_{wn_i}^{m+1} a_{wn_{i-1}}^{m+1} \right)$$
(A.17)

$$-\zeta_{e_{win}} \left(S_{w_i}^{m+1} - S_{w_i}^m \right) = 0$$

where

$$\zeta = \frac{V_b}{\Delta t} \tag{A.18}$$

and,

$$T_{a_{wn}} = \frac{\kappa A}{4\Delta x} \tag{A.19}$$

and,

$$\zeta_{e_{wn}} = \frac{e_{wn}V_b}{\Delta t} \tag{A.20}$$

For all the middle gridblocks (1 < i < N), Eqs. (A.17), (A.7) (with the modification of p_c^{m+1} instead of p_c^m), and (A.8) are valid. The system of equations for the *extended model* reveals that Eq. (A.5) calculates p_c^{m+1} , Eq. (A.6) calculates S_c^{m+1} , and Eq. (A.16) calculates p_c^{m+1} . Following block-centered discretization, the boundary conditions outlined in Eq. (17) are applied to the first gridblock, signifying that p_{c_1} and S_{w_1} are already determined for all time steps. It also means that $a_{wn_1}^{m+1} = a_{wn_1}^m = a_{wn_1}$ for all time steps. Therefore, Eq. (A.5) should be rewritten for the first gridblock in the *extended model* as:

$$T_{w_{1,2}} \left(p_{n_2}^{m+1} - p_{n_1}^{m+1} \right) - T_{w_{1,2}} \left(p_{c_2}^{m+1} - p_{c_1}^{m+1} \right)^{p_{c_0}}$$

$$-\zeta_{w_1} S_{w_1}^{m+1} + \zeta_{w_1} S_{w_1}^{m} + g_{w}^{q_{w_{inj}}} = 0$$
(A.21)

and, Eq. (A.16) for the first gridblock is turned into:

$$-T_{a_{wn}}\left(a_{wn_2}^{m+1^2} + 4a_{wn_1}a_{wn_2}^{m+1} - 8a_{wn_1}^2\right) = 0 \tag{A.22}$$

Based on the conditions described in Eq. (10), both Eq. (A.12) and (A.13) remain valid for the last gridblock in the *extended model*. By taking advantages of the *reflection technique* [14], Eq. (A.16) for the last gridblock can be expressed as:

$$\zeta \left(a_N^{m+1} - a_N^m \right) - T_{a_{wn}} \left(a_{wn_{N-1}}^{m+1^2} - 8a_{wn_N}^{m+1^2} + 4a_{wn_N}^{m+1} a_{wn_{N-1}}^{m+1} \right) - \zeta_{e_{wn}} \left(S_{wn}^{m+1} - S_{wn}^m \right) = 0$$
(A.23)

Overall, writing Eqs. (A.7), (A.8), (A.17), (A.21), (A.22), (A.12), (A.13), and (A.23) for N gridblocks in the *extended model* results in a set of 3N-2 nonlinear simultaneous algebraic equations (F) that for a proper set of p_n , S_w and p_c should generate 3N-2 zeros, or:

$$F\left(X_{3N-2}^{m+1}\right) = [0]_{3N-2} \tag{A.24}$$

References

- [1] A. Herring, C. Sun, R. Armstrong, M. Saadatfar, Insights into wettability alteration during cyclic scCO2-brine injections in a layered Bentheimer sandstone, Int. J. Greenh. Gas Control 122 (2023) 103803, http://dx.doi.org/10.1016/j.ijggc.2022.103803.
- [2] A. Najafi, J. Siavashi, M. Ebadi, D. Orlov, M. Sharifi, J. Fahimpour, M.K. Moraveji, D. Koroteev, Using computational fluid dynamics to compute the pore-scale CO2-brine relative permeability, Fuel 341 (2023) 127715, http://dx.doi.org/10.1016/j.fuel.2023.127715.
- [3] M.E. Zayed, B. Shboul, H. Yin, J. Zhao, A.A. Zayed, Recent advances in geothermal energy reservoirs modeling: Challenges and potential of thermo-fluid integrated models for reservoir heat extraction and geothermal energy piles design, J. Energy Storage 62 (2023) 106835, http://dx.doi.org/10.1016/j.est. 2023.106835.

- [4] Y. Bezyan, M. Ebadi, S. Gerami, R. Rafati, M. Sharifi, D. Koroteev, A novel approach for solving nonlinear flow equations: The next step towards an accurate assessment of shale gas resources, Fuel 236 (2019) 622–635, http://dx.doi.org/10.1016/j.fuel.2018.08.157.
- [5] R. Zagorščak, N. An, R. Palange, M. Green, M. Krishnan, H.R. Thomas, Underground coal gasification A numerical approach to study the formation of syngas and its reactive transport in the surrounding strata. Fuel 253 (2019) 349–360. http://dx.doi.org/10.1016/j.fuel.2019.04.164.
- [6] Y.A. Alzahid, P. Mostaghimi, S.D. Walsh, R.T. Armstrong, Flow regimes during surfactant flooding: The influence of phase behaviour, Fuel 236 (2019) 851–860. http://dx.doi.org/10.1016/i.fuel.2018.08.086.
- [7] D. Zhang, Two-phase flow, in: Stochastic Methods for Flow in Porous Media, Elsevier, 2002, pp. 262–296, http://dx.doi.org/10.1016/b978-012779621-5/50007-3.
- [8] S. Geiger, K.S. Schmid, Y. Zaretskiy, Mathematical analysis and numerical simulation of multi-phase multi-component flow in heterogeneous porous media, Curr. Opin. Colloid Interface Sci. 17 (3) (2012) 147–155, http://dx.doi.org/10.1016/j.cocis.2012.01.003.
- [9] J.R. Fanchi, Fundamentals of reservoir simulation, in: Principles of Applied Reservoir Simulation, Elsevier, 2018, pp. 163–179, http://dx.doi.org/10.1016/b978-0-12-815563-9.00009-4.
- [10] A.Y. Dandekar, Petroleum Reservoir Rock and Fluid Properties, second ed., CRC Press, 2013.
- [11] A. Tarek, Reservoir Engineering Handbook, fifth ed., Elsevier, 2018.
- [12] C.J. van Duijn, K. Mitra, Hysteresis and horizontal redistribution in porous media, Transp. Porous Media 122 (2) (2018) 375–399, http://dx.doi.org/10. 1007/s11242-018-1009-2.
- [13] R.T. Armstrong, M.L. Porter, D. Wildenschild, Linking pore-scale interfacial curvature to column-scale capillary pressure, Adv. Water Resour. 46 (2012) 55–62, http://dx.doi.org/10.1016/j.advwatres.2012.05.009.
- [14] J. Abou-Kassem, M.R. Islam, S. Farouq-Ali, Petroleum Reservoir Simulation: The Engineering Approach, second ed., Gulf Professional Publishing, 2020.
- [15] V. Joekar-Niasar, F. Doster, R.T. Armstrong, D. Wildenschild, M.A. Celia, Trapping and hysteresis in two-phase flow in porous media: A pore-network study, Water Resour. Res. 49 (7) (2013) 4244–4256, http://dx.doi.org/10.1002/wrcr.20313.
- [16] M.A. Elhaj, M.E. Hossain, S.A. Imtiaz, G.F. Naterer, Hysteresis of wettability in porous media: A review, J. Petrol. Explor. Prod. Technol. 10 (5) (2020) 1897–1905, http://dx.doi.org/10.1007/s13202-020-00872-x.
- [17] M.A. Elhaj, M.I. Miah, M.E. Hossain, State-of-the-art on capillary pressure hysteresis: Productive techniques for better reservoir performance, Upstream Oil Gas Technol. 7 (2021) 100040, http://dx.doi.org/10.1016/j.upstre.2021.100040.
- [18] S. Hassanizadeh, W.G. Gray, Mechanics and thermodynamics of multiphase flow in porous media including interphase boundaries, Adv. Water Resour. 13 (4) (1990) 169–186, http://dx.doi.org/10.1016/0309-1708(90)90040-b.
- [19] S.M. Hassanizadeh, W.G. Gray, Toward an improved description of the physics of two-phase flow, Adv. Water Resour. 16 (1) (1993) 53–67, http://dx.doi.org/10.1016/0309-1708(93)90029-f.
- [20] W.G. Gray, S.M. Hassanizadeh, Unsaturated flow theory including interfacial phenomena, Water Resour. Res. 27 (8) (1991) 1855–1863, http://dx.doi.org/ 10.1029/91wr01260.
- [21] W.G. Gray, S.M. Hassanizadeh, Paradoxes and realities in unsaturated flow theory, Water Resour. Res. 27 (8) (1991) 1847–1854, http://dx.doi.org/10. 1029/91wr01259.
- [22] R.T. Armstrong, A. Georgiadis, H. Ott, D. Klemin, S. Berg, Critical capillary number: Desaturation studied with fast X-ray computed microtomography, Geophys. Res. Lett. 41 (1) (2014) 55–60, http://dx.doi.org/10.1002/2013gl058075.
- [23] S.V. Dastjerdi, N. Karadimitriou, S.M. Hassanizadeh, H. Steeb, Experimental evaluation of fluid connectivity in two-phase flow in porous media, Adv. Water Resour. 172 (2023) 104378, http://dx.doi.org/10.1016/j.advwatres.2023.104378.
- [24] V. Joekar-Niasar, S.M. Hassanizadeh, Uniqueness of Specific Interfacial Area-capillary pressure-saturation relationship under non-equilibrium conditions in two-phase porous media flow, Transp. Porous Media 94 (2) (2012) 465–486, http://dx.doi.org/10.1007/s11242-012-9958-3.
- [25] V. Joekar-Niasar, S.M. Hassanizadeh, A. Leijnse, Insights into the relationships among capillary pressure, saturation, interfacial area and relative permeability using pore-network modeling, Transp. Porous Media 74 (2) (2007) 201–219, http://dx.doi.org/10.1007/s11242-007-9191-7.
- [26] S.V. Dastjerdi, N. Karadimitriou, S.M. Hassanizadeh, H. Steeb, Experimental evaluation of fluid connectivity in two-phase flow in porous media during drainage, Water Resour. Res. 58 (11) (2022) http://dx.doi.org/10.1029/2022wr033451.
- [27] M.L. Porter, M.G. Schaap, D. Wildenschild, Lattice-Boltzmann simulations of the capillary pressure–saturation–interfacial area relationship for porous media, Adv. Water Resour. 32 (11) (2009) 1632–1640, http://dx.doi.org/10.1016/j.advwatres.2009.08.009.
- [28] M.L. Porter, D. Wildenschild, G. Grant, J.I. Gerhard, Measurement and prediction of the relationship between capillary pressure, saturation, and interfacial area in a NAPL-water-glass bead system, Water Resour. Res. 46 (8) (2010) http://dx.doi.org/10.1029/2009wr007786.
- [29] P.C. Reeves, M.A. Celia, A functional relationship between capillary pressure, saturation, and interfacial area as revealed by a pore-scale network model, Water Resour. Res. 32 (8) (1996) 2345–2358, http://dx.doi.org/10.1029/96wr01105.
- [30] R.J. Held, M.A. Celia, Modeling support of functional relationships between capillary pressure, saturation, interfacial area and common lines, Adv. Water Resour. 24 (3-4) (2001) 325-343, http://dx.doi.org/10.1016/s0309-1708(00)00060-9.
- [31] J.-T. Cheng, Linking pressure and saturation through interfacial areas in porous media, Geophys. Res. Lett. 31 (8) (2004) http://dx.doi.org/10.1029/2003e1019282.
- [32] D. Chen, L.J. Pyrak-Nolte, J. Griffin, N.J. Giordano, Measurement of interfacial area per volume for drainage and imbibition, Water Resour. Res. 43 (12) (2007) http://dx.doi.org/10.1029/2007wr006021.
- [33] J.O. Helland, S.M. Skjaeveland, Relationship between capillary pressure, saturation, and interfacial area from a model of mixed-wet triangular tubes, Water Resour. Res. 43 (12) (2007) http://dx.doi.org/10.1029/2006wr005698.
- [34] Y. Liu, D.D. Nolte, L.J. Pyrak-Nolte, Hysteresis and interfacial energies in smooth-walled microfluidic channels, Water Resour. Res. 47 (1) (2011) http://dx.doi.org/10.1029/2010wr009541.
- [35] J.E. McClure, M.A. Berrill, W.G. Gray, C.T. Miller, Influence of phase connectivity on the relationship among capillary pressure, fluid saturation, and interfacial area in two-fluid-phase porous medium systems, Phys. Rev. E 94 (3) (2016) http://dx.doi.org/10.1103/physreve.94.033102.
- [36] R.T. Armstrong, J.E. McClure, V. Robins, Z. Liu, C.H. Arns, S. Schlüter, S. Berg, Porous media characterization using Minkowski functionals: Theories, applications and future directions, Transp. Porous Media 130 (1) (2018) 305–335, http://dx.doi.org/10.1007/s11242-018-1201-4.
- [37] S. Schlüter, S. Berg, M. Rücker, R.T. Armstrong, H.-J. Vogel, R. Hilfer, D. Wildenschild, Pore-scale displacement mechanisms as a source of hysteresis for two-phase flow in porous media, Water Resour. Res. 52 (3) (2016) 2194–2205, http://dx.doi.org/10.1002/2015wr018254.
- [38] J.E. McClure, R.T. Armstrong, M.A. Berrill, S. Schlüter, S. Berg, W.G. Gray, C.T. Miller, Geometric state function for two-fluid flow in porous media, Phys. Rev. Fluids 3 (8) (2018) http://dx.doi.org/10.1103/physrevfluids.3.084306.
- [39] C.T. Miller, K. Bruning, C.L. Talbot, J.E. McClure, W.G. Gray, Nonhysteretic capillary pressure in two-fluid porous medium systems: Definition, evaluation, validation, and dynamics, Water Resour. Res. 55 (8) (2019) 6825–6849, http://dx.doi.org/10.1029/2018wr024586.
- [40] J.E. McClure, M.A. Berrill, W.G. Gray, C.T. Miller, Tracking interface and common curve dynamics for two-fluid flow in porous media, J. Fluid Mech. 796 (2016) 211–232, http://dx.doi.org/10.1017/jfm.2016.212.
- [41] V. Joekar-Niasar, S.M. Hassanizadeh, Specific interfacial area: The missing state variable in two-phase flow equations? Water Resour. Res. 47 (5) (2011) http://dx.doi.org/10.1029/2010wr009291.

- [42] J.E. McClure, T. Ramstad, Z. Li, R.T. Armstrong, S. Berg, Modeling geometric state for fluids in porous media: Evolution of the Euler characteristic, Transp. Porous Media 133 (2) (2020) 229–250. http://dx.doi.org/10.1007/s11242-020-01420-1.
- [43] D.E. Meisenheimer, J.E. McClure, M.L. Rivers, D. Wildenschild, Exploring the effect of flow condition on the constitutive relationships for two-phase flow, Adv. Water Resour. 137 (2020) 103506, http://dx.doi.org/10.1016/j.advwatres.2020.103506.
- [44] J. Niessner, S.M. Hassanizadeh, A model for two-phase flow in porous media including fluid-fluid interfacial area, Water Resour. Res. 44 (8) (2008) http://dx.doi.org/10.1029/2007wr006721.
- [45] I. Pop, C. van Duijn, J. Niessner, S. Hassanizadeh, Horizontal redistribution of fluids in a porous medium: The role of interfacial area in modeling hysteresis, Adv. Water Resour. 32 (3) (2009) 383–390, http://dx.doi.org/10.1016/j.advwatres.2008.12.006.
- [46] J. Niessner, S. Berg, S.M. Hassanizadeh, Comparison of two-phase Darcy's law with a thermodynamically consistent approach, Transp. Porous Media 88 (1) (2011) 133–148, http://dx.doi.org/10.1007/s11242-011-9730-0.
- [47] J. Niessner, S.M. Hassanizadeh, D. Crandall, Modeling two-phase flow in porous media including fluid-fluid interfacial area, in: Volume 12: Mechanics of Solids, Structures and Fluids, ASMEDC, 2008, http://dx.doi.org/10.1115/imece2008-66098.
- [48] J. Bear, Dynamics of Fluids in Porous Media, Dover Publications, 1988.
- [49] D. Tiab, E.C. Donaldson, Capillary pressure, in: Petrophysics, Elsevier, 2016, pp. 279-317, http://dx.doi.org/10.1016/b978-0-12-803188-9.00005-x.
- [50] R.H. Brooks, A.T. Corey, Properties of porous media affecting fluid flow, J. Irrigation Drainage Div. 92 (2) (1966) 61–88, http://dx.doi.org/10.1061/jrcea4.0000425.
- [51] S.C. Chapra, Canale, Numerical Methods for Engineers, eighth ed., McGraw-Hill, 2021.
- [52] A. Gilat, V. Subramaniam, Numerical Methods for Engineers and Scientists: An Introduction with Applications using MATLAB, eighth ed., Wiley Publishing, 2007.
- [53] J. Sheldon, W. Cardwell, One-dimensional, incompressible, noncapillary, two-phase fluid flow in a porous medium, Trans. AIME 216 (01) (1959) 290–296, http://dx.doi.org/10.2118/978-g.
- [54] C. Redondo, G. Rubio, E. Valero, On the efficiency of the IMPES method for two phase flow problems in porous media, J. Pet. Sci. Eng. 164 (2018) 427–436, http://dx.doi.org/10.1016/j.petrol.2018.01.066.
- [55] T. Ertekin, J.H. Abou-Kassem, G.R. King, Basic Applied Reservoir Simulation, Society of Petroleum Engineers, 2001.
- [56] S. Buckley, M. Leverett, Mechanism of fluid displacement in sands, Trans. AIME 146 (01) (1942) 107-116, http://dx.doi.org/10.2118/942107-g.
- [57] S.M. Hassanizadeh, W.G. Gray, Thermodynamic basis of capillary pressure in porous media, Water Resour. Res. 29 (10) (1993) 3389–3405, http://dx.doi.org/10.1029/93wr01495.
- [58] L.C. Evans, Partial Differential Equations, second ed., American Mathematical Society, 2010.
- [59] H.F. Nordhaug, H.K. Dahle, M.S. Espedal, W.G. Gray, M.A. Celia, Two Phase Flow Including Interfacial Area as a Variable, The XIII international conference on computational methods in water resources, 2000.
- [60] P. Deuflhard, Newton Methods for Nonlinear Problems: Affine Invariance and Adaptive Algorithms, Springer Science & Business Media, 2011.
- [61] D.V. Voskov, H.A. Tchelepi, Comparison of nonlinear formulations for two-phase multi-component EoS based simulation, J. Pet. Sci. Eng. 82–83 (2012) 101–111, http://dx.doi.org/10.1016/j.petrol.2011.10.012.
- [62] P.K. Deb, F. Akter, S.A. Imtiaz, M.E. Hossain, Nonlinearity and solution techniques in reservoir simulation: A review, J. Nat. Gas Sci. Eng. 46 (2017) 845–864, http://dx.doi.org/10.1016/j.jngse.2017.07.031.
- [63] W.H. Press, S.A. Teukolsky, W.T. Vetterling, B.P. Flannery, Numerical Recipes in C: The Art of Scientific Computing, third ed., Cambridge University Press, 2007.
- [64] H.-B. An, J. Wen, T. Feng, On finite difference approximation of a matrix-vector product in the Jacobian-free Newton-Krylov method, J. Comput. Appl. Math. 236 (6) (2011) 1399–1409, http://dx.doi.org/10.1016/j.cam.2011.09.003.
- [65] A. Paszke, S. Gross, F. Massa, A. Lerer, J. Bradbury, G. Chanan, T. Killeen, Z. Lin, N. Gimelshein, L. Antiga, A. Desmaison, A. Köpf, E. Yang, Z. DeVito, M. Raison, A. Tejani, S. Chilamkurthy, B. Steiner, L. Fang, J. Bai, S. Chintala, PyTorch: An Imperative Style, High-Performance Deep Learning Library, arXiv, 2019, http://dx.doi.org/10.48550/ARXIV.1912.01703.
- [66] A.E. Peksa, K.-H.A. Wolf, P.L. Zitha, Bentheimer sandstone revisited for experimental purposes, Mar. Pet. Geol. 67 (2015) 701–719, http://dx.doi.org/10.1016/j.marpetgeo.2015.06.001.
- [67] I. Shikhov, M.N. d'Eurydice, J.-Y. Arns, C.H. Arns, An experimental and numerical study of relative permeability estimates using spatially resolved t₁-z NMR, Transp. Porous Media 118 (2) (2017) 225–250, http://dx.doi.org/10.1007/s11242-017-0855-7.
- [68] H. Abdoulghafour, M. Sarmadivaleh, L.P. Hauge, M. Fernø, S. Iglauer, Capillary pressure characteristics of CO2-brine-sandstone systems, Int. J. Greenh. Gas Control 94 (2020) 102876, http://dx.doi.org/10.1016/j.ijggc.2019.102876.
- [69] P. Virtanen, R. Gommers, T.E. Oliphant, M. Haberland, T. Reddy, D. Cournapeau, E. Burovski, P. Peterson, W. Weckesser, J. Bright, S.J. van der Walt, M. Brett, J. Wilson, K.J. Millman, N. Mayorov, A.R.J. Nelson, E. Jones, R. Kern, E. Larson, C.J. Carey, İ. Polat, Y. Feng, E.W. Moore, J. VanderPlas, D. Laxalde, J. Perktold, R. Cimrman, I. Henriksen, E.A. Quintero, C.R. Harris, A.M. Archibald, A.H. Ribeiro, F. Pedregosa, P. van Mulbregt, Author correction: SciPy 1.0: Fundamental algorithms for scientific computing in python, Nature Methods 17 (3) (2020) 352, http://dx.doi.org/10.1038/s41592-020-0772-5.
- [70] S. Mukherjee, R.T. Johns, S. Foroughi, M.J. Blunt, Fluid-Fluid Interfacial Area and its impact on relative permeability: A pore network modeling study, SPE J. 28 (02) (2022) 653–663, http://dx.doi.org/10.2118/209445-pa.
- [71] R. Courant, K. Friedrichs, H. Lewy, Über die partiellen differenzengleichungen der mathematischen physik, Math. Ann. 100 (1) (1928) 32–74, http://dx.doi.org/10.1007/bf01448839.
- [72] K. Coats, IMPES stability: The CFL limit, in: SPE Reservoir Simulation Symposium, Houston, Texas, USA, 2001, http://dx.doi.org/10.2118/66345-ms.
- [73] J. Franc, P. Horgue, R. Guibert, G. Debenest, Benchmark of different CFL conditions for IMPES, Comptes Rendus Mécanique 344 (10) (2016) 715–724, http://dx.doi.org/10.1016/j.crme.2016.08.003.
- [74] K. Hassan K., Nonlinear Systems, third ed., P&C ECS, 2001.
- [75] C.R. Harris, K.J. Millman, S.J. van der Walt, R. Gommers, P. Virtanen, D. Cournapeau, E. Wieser, J. Taylor, S. Berg, N.J. Smith, R. Kern, M. Picus, S. Hoyer, M.H. van Kerkwijk, M. Brett, A. Haldane, J.F. del Río, M. Wiebe, P. Peterson, P. Gérard-Marchant, K. Sheppard, T. Reddy, W. Weckesser, H. Abbasi, C. Gohlke, T.E. Oliphant, Array programming with NumPy, Nature 585 (7825) (2020) 357–362, http://dx.doi.org/10.1038/s41586-020-2649-2.